

ARTICLE

DOI: 10.1038/s42004-018-0064-5

OPEN

# Intercalated metal–organic frameworks with high electronic conductivity as negative electrode materials for hybrid capacitors

Yuka Ozawa<sup>1</sup>, Nobuhiro Ogihara <sup>1</sup>, Masaki Hasegawa<sup>1</sup>, Osamu Hiruta<sup>1</sup>, Nobuko Ohba <sup>1</sup> & Yoshihiro Kishida<sup>1</sup>

Hybrid capacitors should ideally exhibit high volumetric energy density, favorable low-temperature performance and safe operation. Here we describe a negative electrode comprising an intercalated metal–organic framework, 4,4'-biphenyl dicarboxylate dilithium [4,4'-Bph(COOLi)<sub>2</sub>], which forms a repeating organic–inorganic layered structure of  $\pi$ -stacked biphenyl and tetrahedral LiO<sub>4</sub> units. The electrode shows a stepwise two-electron transfer and has a capacity of 190 mAh g<sup>-1</sup> at 0.7 V vs. Li/Li<sup>+</sup>, which can suppress the lithium metal deposition reaction occurring an internal short circuit. A hybrid capacitor containing 4,4'-Bph(COOLi)<sub>2</sub> negative and activated carbon positive electrodes possesses high volumetric energy density of approximately 60 Wh L<sup>-1</sup> and good high-rate performance, particularly at the low temperature of 0 °C, because of low charge-transfer resistance along with low activation energy. Hopping mobility calculations suggest the observed low resistance properties are the result of high electron mobility arising from two electron-hopping pathways between adjacent molecules in the  $\pi$ -stacked biphenyl packing layer by lithium intercalation.

<sup>1</sup>Toyota Central R&D Laboratories, Inc., Nagakute, Aichi 480-1192, Japan. These authors contributed equally: Yuka Ozawa, Nobuhiro Ogihara. Correspondence and requests for materials should be addressed to N.O. (email: [ogihara@mosk.tytlabs.co.jp](mailto:ogihara@mosk.tytlabs.co.jp))

Electrochemical capacitors (i.e., supercapacitors) with high-energy densities have promising applications for load leveling in electric, hybrid, and fuel-cell vehicles<sup>1</sup>, solar and wind power generation systems<sup>2</sup>, and micro-scale applications such as wearable devices, radio-frequency identification tags, and on-chip energy devices<sup>3</sup>. Electric double-layer capacitors (EDLCs), which are principal electrochemical capacitors that use identical activated carbon (AC) electrodes with microporous and high specific surface areas, show fast charge–discharge characteristics, remarkable stability, long cycle life, and safety because they utilize non-faradaic electric double-layer formation as a charge-storage mechanism<sup>4,5</sup>. However, EDLCs are only applied as limiting energy suppliers because of their moderate energy densities ( $\sim 10 \text{ Wh L}^{-1}$ ) resulting from the low capacitance and operating cell voltage (0–2.5 V)<sup>5</sup>. Hybrid capacitors comprised of non-faradaic capacitor-type and faradaic battery-type electrodes have emerged in recent years as high-energy electrochemical capacitors. Li-ion capacitors (LICs) with activated carbon as the positive electrode and Li-doped graphite carbon as the negative electrode have been reported<sup>6,7</sup>. The energy densities of these LICs ( $\sim 50 \text{ Wh L}^{-1}$ ) are approximately five times larger than those of EDLCs because of their higher operating cell voltage (1.5–3.8 V) and large capacity utilization range, which can be attributed to the Li doping<sup>4</sup>.

For large-scale applications, it is necessary to develop electrochemical capacitors with high-energy density while maintaining the safety. However, in existing LICs that use graphite as the negative electrode operating at a potential of 0.05 V vs. Li/Li<sup>+</sup>, the deposition of metallic Li dendrites can cause internal short circuits between the positive and negative electrodes at high charging rates and/or low temperatures<sup>8,9</sup>. To address this safety issue, we proposed to control the negative electrode potential using aromatic dicarboxylate Li salts, which operate at potentials ranging from 0.5 to 1.0 V<sup>10,11</sup>. Because these carboxylate salts are abundant, low cost, and environmentally friendly, many groups have used them in the negative electrodes of lithium and sodium batteries<sup>12–18</sup>.

Our group first reported aromatic dicarboxylate lithium salts as electrode materials that operate at 0.8 V and investigated the change in crystalline structure during Li intercalation<sup>10,11</sup>. 2,6-naphthalene dicarboxylate dilithium [2,6-Naph(COOLi)<sub>2</sub>], a representative crystalline aromatic dicarboxylate lithium salt, was found to form an organic–inorganic layered metal–organic framework (MOF). The 2,6-Naph(COOLi)<sub>2</sub> electrode exhibited reversible lithium intercalation with the transfer of two electrons and two Li<sup>+</sup> ions, corresponding to a reversible capacity of 221 mAh g<sup>-1</sup> at a flat potential of 0.8 V vs. Li/Li<sup>+</sup><sup>19–21</sup>. The framework was maintained during lithium intercalation with a remarkably small change in volume (0.33%); therefore, we named the series of electrochemically active MOFs as “intercalated MOFs (iMOFs)”. The redox reaction can be improved by controlling the crystal orientation by heat treatment<sup>20</sup> and controlling the crystal plane using synthetic solvents.<sup>22</sup> The hybrid capacitor with 2,6-Naph(COOLi)<sub>2</sub> and activated carbon as the negative and positive electrodes, respectively, exhibits a high-energy density of approximately 60 Wh L<sup>-1</sup>, high-power density, and good cyclability<sup>21</sup>.

To obtain iMOF-based hybrid capacitors with high-power capability and low-temperature performance, the high-rate characteristics of iMOF electrode materials must be further improved. Although some reports have focused on the iMOF electrode with high-rate capability<sup>18,23</sup>, the high-rate performance at temperatures lower than 0 °C and its mechanism of the high-rate performance remain to be elucidated. To design an iMOF electrode that provides low resistance and favorable low-temperature characteristics, we selected a dicarboxylate lithium

salt containing a biphenyl (Bph) framework<sup>10,11</sup> based on the following characteristics: (i) stepwise formation of a stable complex with one and two lithium atoms per unit (Li<sup>-</sup> Bph<sup>-</sup> and Li<sup>2-</sup> Bph<sup>2-</sup>, respectively)<sup>24</sup>; (ii) further stabilization of lithium through coordination with oxygen<sup>24,25</sup>; and (iii) expectation of a lower reduction potential of the biphenyl dicarboxylate lithium salt than that of the naphthalene because biphenyl exhibits a lower reduction potential than naphthalene (0.45 V vs. Li/Li<sup>+</sup> for biphenyl compared to 0.51 V vs. Li/Li<sup>+</sup> for naphthalene)<sup>26</sup>. The electrochemical behavior of this material has already been reported as a preliminary step<sup>23</sup>. The mechanism of electronic conduction, which greatly contributes to the low resistance of this material, was not detailed in the report.

In this paper, we focus on understanding the detailed electrochemical behavior of 4,4'-biphenyl dicarboxylate dilithium salt [4,4'-Bph(COOLi)<sub>2</sub>] and demonstrate its potential as a low-resistance iMOF electrode material that can achieve high-rate (approximately 1 min discharge) and low-temperature performance (0 °C) in hybrid capacitors. Electrochemical impedance spectroscopy and calculations of electro-hopping mobility reveal that the mechanism of electronic conduction enables low resistance along with favorable low-temperature performance.

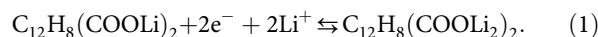
## Results

**Characterization of 4,4'-Bph(COOLi)<sub>2</sub> crystals.** The powder X-ray diffraction (XRD) pattern of 4,4'-Bph(COOLi)<sub>2</sub> and the corresponding Rietveld refinement (Fig. 1a) revealed a repeating organic–inorganic layered structure of organic  $\pi$ -stacked biphenyl units and inorganic tetrahedral LiO<sub>4</sub> units (Fig. 1a, inset). A previous paper reported that this structure is almost insoluble in any of the common organic electrolyte<sup>27</sup>. The structure has the same space group as the previously reported 2,6-Naph(COOLi)<sub>2</sub><sup>19</sup>. We also obtained a reasonable Fourier map of the crystal structure (Fig. 1b). Compared with 2,6-Naph(COOLi)<sub>2</sub>, 4,4'-Bph(COOLi)<sub>2</sub> was found to have a longer lattice parameter in the *a*-axis direction corresponding to the organic–inorganic stack direction because of the longer aromatic biphenyl unit of 4,4'-Bph(COOLi)<sub>2</sub>; the same lattice parameters in the *b*- and *c*-axis directions (corresponding to the stack surface direction) (Supplementary Table 1)<sup>28</sup>. Scanning electron microscopy (SEM) images (Supplementary Figure 1) indicated that 4,4'-Bph(COOLi)<sub>2</sub> powder was obtained as an agglomerate with small particles. The primary particles (ca. 2–5  $\mu\text{m}$ , Supplementary Figure 1a, b) were smaller than the previously reported 2,6-Naph(COOLi)<sub>2</sub> particles (approximately >10  $\mu\text{m}$ , Supplementary Figure 1c, d)<sup>19</sup>.

**Electrochemical characterization.** We characterized the electrochemical behavior of a 4,4'-Bph(COOLi)<sub>2</sub> electrode in a coin-type cell using Li metal as the counter electrode. We fabricated the 4,4'-Bph(COOLi)<sub>2</sub> electrode with amphiphilic polymer binders because we have successfully prepared a high-capacity electrode for aromatic dicarboxylate lithium salts using amphiphilic polymer binders (e.g., carboxymethylcellulose and polyacrylic acid); in the resulting self-assembled electrode, the active materials were uniformly covered with conducting carbon, leading to high electro-activity. First, cyclic voltammetry (CV) was performed to confirm the electrochemical behavior and reversibility of the proposed material. The CV responses, as shown in Supplementary Figure 2a, b, exhibited a reversible redox couple. The redox potential of the 4,4'-Bph(COOLi)<sub>2</sub> electrode was ca. 0.7 V vs. Li/Li<sup>+</sup>, which is ca. 0.1 V lower than that of the 2,6-Naph(COOLi)<sub>2</sub> electrode (ca. 0.8 V vs. Li/Li<sup>+</sup>), as shown in Supplementary Figure 2c and agrees well with the prediction from the reduction potential of the aromatic unit shown in the above

concept<sup>26</sup>. Next, the reversible specific capacity was determined from the galvanostatic charge–discharge measurement. As shown in Supplementary Figure 3, the charge/discharge curve of a Li/4,4'-Bph(COOLi)<sub>2</sub> cell showed a reversible specific capacity of ca. 190 mAh g<sup>-1</sup>, although there is an initial irreversible capacity related to decomposition of electrolyte<sup>19</sup>. As shown in Fig. 2a, the

reversible capacity derives approximately 2Li<sup>+</sup> ion transfer per molecule corresponding to almost the same theoretical specific capacity (200 mAh g<sup>-1</sup>) as shown in the following redox reaction:



Moreover, the 4,4'-Bph(COOLi)<sub>2</sub> electrode exhibited a small polarization of ca. 40 mV at deep depth of discharge (DOD) of the electrode and a large polarization of ca. 260 mV at shallow DOD. As shown in Fig. 2b, differential capacity ( $dQ/dV$ ) plots calculated from the charge/discharge curves of the same cells showed good agreement with the CV results and revealed a clear and further detailed potential changes. The  $dQ/dV$  plots indicate two redox couples at a potential of approximately 0.7 V and one broad peak at a potential of approximately 1 V during discharge in the 4,4'-Bph(COOLi)<sub>2</sub> electrode (Fig. 2b, inset); in contrast, only one redox couple is observed for the 2,6-Naph(COOLi)<sub>2</sub> electrode at 0.8 V. This suggests that a stepwise two-electron transfer occurs in the 4,4'-Bph(COOLi)<sub>2</sub> electrode, whereas a concerted two-electron transfer occurs in the 2,6-Naph(COOLi)<sub>2</sub> electrode. Since the formation of one-electron reduced anion radical biphenyl (Bph<sup>•-</sup>)<sup>24, 25</sup> and two-electron reduced dianion biphenyl (Bph<sup>2-</sup>)<sup>29,30</sup> has been reported in the biphenyl framework, such stepwise behavior observed in the  $dQ/dV$  plot of 4,4'-Bph(COOLi)<sub>2</sub> electrode is assumed to be a redox reaction via the anion radical biphenyl (Bph<sup>•-</sup>) and dianion biphenyl (Bph<sup>2-</sup>).

**Optical bandgaps.** To understand the polarization behaviors of these electrodes, ultraviolet–visible (UV–vis) spectroscopy was used to determine direct and indirect bandgaps ( $E_g$ ) of a series of aromatic carboxylate dilithium salts, 4,4'-Bph(COOLi)<sub>2</sub>, 2,6-Naph(COOLi)<sub>2</sub>, and 1,4-benzene carboxylate dilithium (1,4-Ph(COOLi)<sub>2</sub>). As shown in Supplementary Figure 4, only 4,4'-Bph(COOLi)<sub>2</sub> showed a broadened UV–vis spectrum in the high wavelength region among the three measured materials. Such broadened spectral behavior has been reported for aromatic compounds with rotatable C–C link<sup>31</sup>. Therefore, the observed broadened spectrum of the 4,4'-Bph(COOLi)<sub>2</sub> indicates the influence of the rotating structure of the biphenyl units inside the crystal.

Direct and indirect bandgaps were estimated from the results of the UV–vis spectra (see Methods). As shown in Fig. 3, the direct bandgap of the 4,4'-Bph(COOLi)<sub>2</sub> ( $E_g = 3.73$  eV in Fig. 3a) was distinctly different from the indirect bandgap ( $E_g = 2.20$  eV in Fig. 3b); in contrast, the direct bandgaps of the 2,6-Naph(COOLi)<sub>2</sub> ( $E_g = 3.26$  eV in Fig. 3c) and 1,4-Ph(COOLi)<sub>2</sub> ( $E_g = 3.93$  eV in Fig. 3e) were nearly the same as the indirect bandgaps of the 2,6-Naph(COOLi)<sub>2</sub> ( $E_g = 3.17$  eV in Fig. 3d) and 1,4-Ph(COOLi)<sub>2</sub> ( $E_g = 3.82$  eV in Fig. 3f). The validity of the direct and

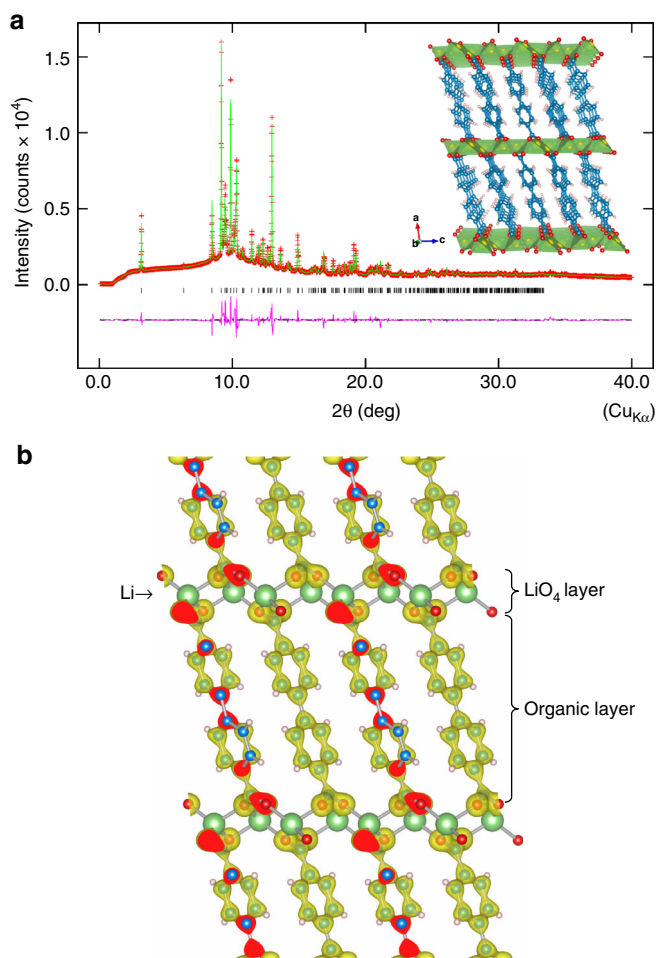


**Fig. 1** Crystal characterization. **a** Rietveld refinement of the powder XRD pattern of 4,4'-Bph(COOLi)<sub>2</sub>: experimental powder XRD pattern (red marks) and calculated powder XRD pattern (green solid line), difference profile (pink solid line), and peak positions (black tick marks). Inset: structure of 4,4'-Bph(COOLi)<sub>2</sub> obtained from the refinement (Li = yellow, O = red, LiO<sub>4</sub> network = green, C = blue, and H = white). **b** Fourier map of the 4,4'-Bph(COOLi)<sub>2</sub> crystal structure obtained from the Rietveld refinement

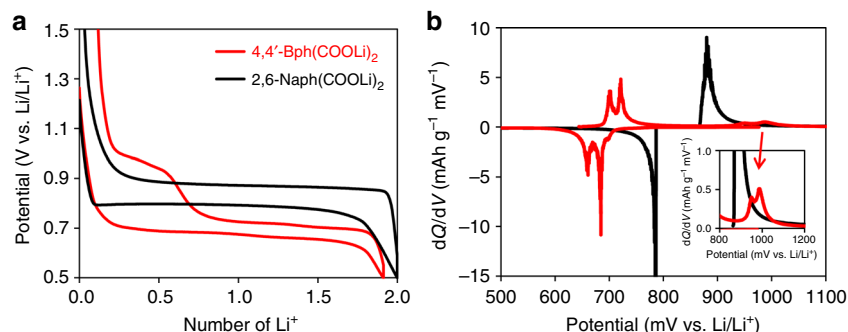


**Fig. 2** Electrochemical characterization. **a** Charge/discharge curves of Li/4,4'-Bph(COOLi)<sub>2</sub> (red) and Li/2,6-Naph(COOLi)<sub>2</sub> (black) cells. **b** Plots of differential capacity ( $dQ/dV$ ) for 4,4'-Bph(COOLi)<sub>2</sub> (red) and 2,6-Naph(COOLi)<sub>2</sub> (black) electrodes calculated from the charge/discharge curves

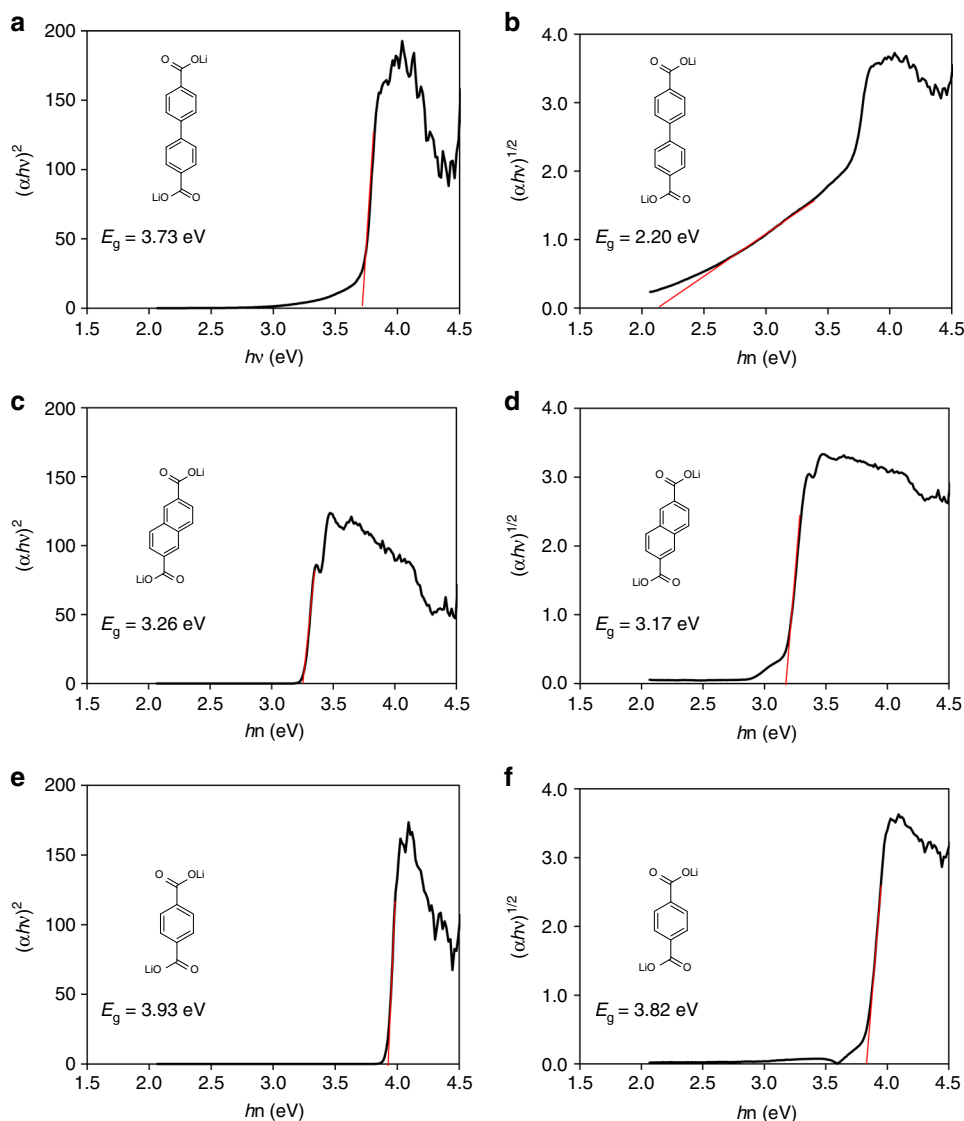


**Fig. 3** Bandgap characterization. Optical bandgaps were obtained from the UV-vis spectra of **a, b** 4,4'-Bph(COOLi)<sub>2</sub>, **c, d** 2,6-Naph(COOLi)<sub>2</sub> and **e, f** 1,4-Ph(COOLi)<sub>2</sub>. The band edges were determined from plots of  $(\alpha h\nu)^{2/n}$  vs.  $h\nu$  with  $n = 1$  (**a, c, e**; indicating direct adsorption) or  $n = 4$  (**b, d, f**; indicating indirect adsorption)

indirect transition of the 4,4'-Bph(COOLi)<sub>2</sub> was investigated from the electronic band structure obtained by calculation (Supplementary Figure 5). In consideration of the previously obtained electronic band structure of the 2,6-Naph(COOLi)<sub>2</sub><sup>32</sup>, these results predict that the excited electrons from valence band maximum (VBM) to conduction-band minimum will be relaxed to VBM via indirect transition for the 4,4'-Bph(COOLi)<sub>2</sub> and direct transition for the 2,6-Naph(COOLi)<sub>2</sub>. Therefore, the electron transition in 4,4'-Bph(COOLi)<sub>2</sub> corresponds to the indirect bandgap of 2.20 eV as well as the direct bandgap of 3.73 eV, whereas the electron transition in 2,6-Naph(COOLi)<sub>2</sub> and 1,4-Ph(COOLi)<sub>2</sub> corresponds to the direct bandgap of 3.26 eV and 3.93 eV, respectively.

This trend in the optical bandgap values, the indirect bandgap of the 4,4'-Bph(COOLi)<sub>2</sub> < the direct bandgap of the 2,6-Naph(COOLi)<sub>2</sub> < the direct bandgap of the 1,4-Ph(COOLi)<sub>2</sub>, agrees well with a previous report on polarization behavior<sup>23</sup>. Thus, this result suggests that low optical bandgap in a series of proposed materials is related to small polarization behavior observed in the charge/discharge curve. In addition, the optical bandgap results also imply that the high direct bandgap of the 4,4'-Bph(COOLi)<sub>2</sub>

is associated with the large polarization at low DOD. These differences are predicted to be related to the planar and twisted moieties in the organic framework. That is, 2,6-Naph(COOLi)<sub>2</sub> and 1,4-Ph(COOLi)<sub>2</sub> maintain the planar structure; in contrast, 4,4'-Bph(COOLi)<sub>2</sub> takes various positions by internal rotation at C–C link connecting benzene units.

**Cell performance of a hybrid capacitor.** Next, we investigated the full-cell performance in a hybrid capacitor using 4,4'-Bph(COOLi)<sub>2</sub> as the negative electrode. A hybrid capacitor with AC as the positive electrode (4,4'-Bph(COOLi)<sub>2</sub>/AC cell) was prepared in a laminate-type cell, as shown in Supplementary Figure 6. 2,6-Naph(COOLi)<sub>2</sub>/AC and graphite/AC cells were also prepared in the same way for comparison. For this capacitor cell fabrication, pre-lithiated treatment was performed. When the pre-lithiated treatment is not performed, as shown in Supplementary Figure 6a, only the electric double-layer capacity of PF<sub>6</sub><sup>-</sup> anions adsorption can be used for the AC-positive electrode. In contrast, by performing the pre-lithiated treatment on the negative electrode, as shown in Supplementary Figure 6b, the capacitor can utilize the electric double-layer capacity of Li<sup>+</sup> cation

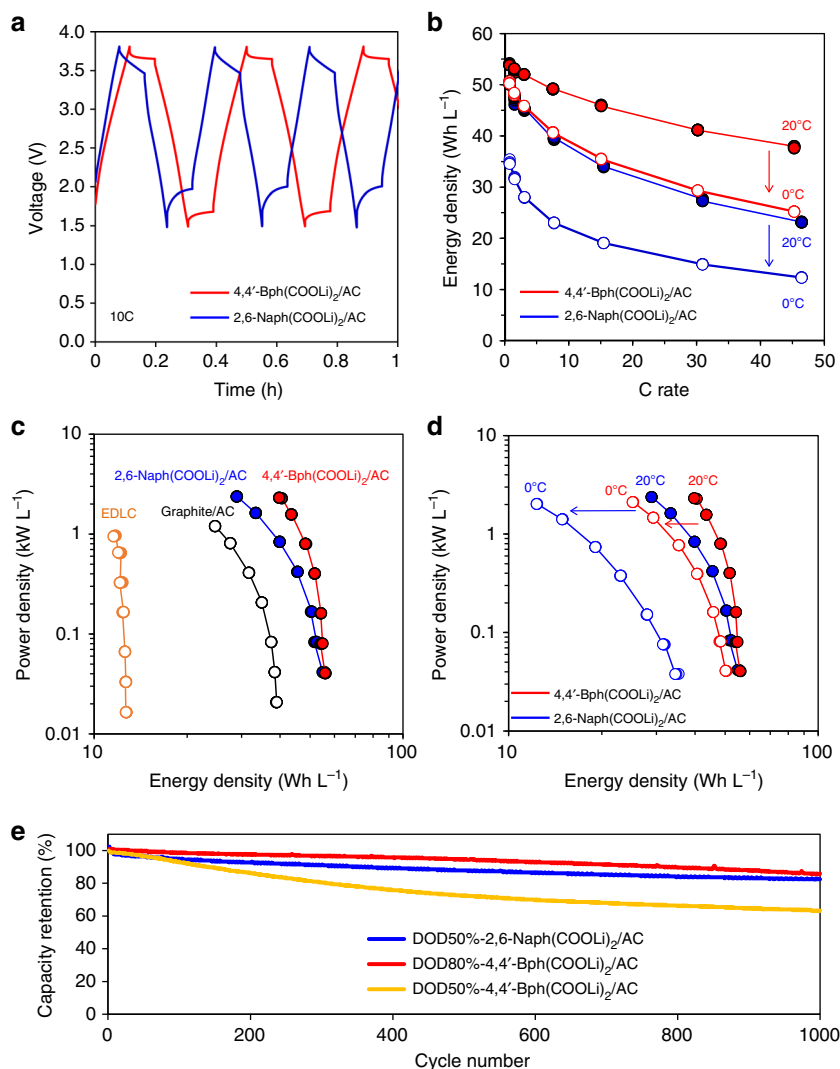


**Fig. 4** Capacitor performances. **a** Charge/discharge curves of 2,6-Naph(COOLi)<sub>2</sub>/AC (blue) and 4,4'-Bph(COOLi)<sub>2</sub>/AC (red) cells with 10 min of rest between charge and discharge. **b** Volumetric energy density vs. C rate for 2,6-Naph(COOLi)<sub>2</sub>/AC (blue) and 4,4'-Bph(COOLi)<sub>2</sub>/AC (red) cells at 0 °C and 20 °C. **c** Ragone plots of EDLC (orange), 2,6-Naph(COOLi)<sub>2</sub>/AC (blue), 4,4'-Bph(COOLi)<sub>2</sub>/AC (red), and graphite/AC (black) cells at 20 °C. Energy density and power density were calculated for the summed volume of negative and positive electrodes. **d** Ragone plots of 2,6-Naph(COOLi)<sub>2</sub>/AC (blue) and 4,4'-Bph(COOLi)<sub>2</sub>/AC (red) cells at 0 °C and 20 °C. **e** Capacity retentions of 2,6-Naph(COOLi)<sub>2</sub> (DOD 50%)/AC (blue), 4,4'-Bph(COOLi)<sub>2</sub> (DOD 50%)/AC (yellow), and 4,4'-Bph(COOLi)<sub>2</sub> (DOD 80%)/AC (red) cells over 1000 cycles

adsorption in addition to that of the PF<sub>6</sub><sup>-</sup> anion adsorption, thereby causing an increase in the capacity of the AC-positive electrode. As a result, the pre-lithiated process results in the design of high-energy density hybrid capacitors. In addition, the pre-lithiated treatment has the object of improving the cell voltage by lowering the potential of the negative electrode in advance and suppressing the influence of the initial irreversible capacity. As shown in Supplementary Figure 7a, the charging and discharging curve of the proposed cell showed typical capacitive behavior in which the voltage varied constantly with respect to the cell capacity. The differential capacity  $dQ/dV$  plots of the charge/discharge plots, as shown in Supplementary Figure 7b, exhibited typical butterfly-type electric double-layer behavior suggesting the use of both Li<sup>+</sup> cations and PF<sub>6</sub><sup>-</sup> anions at the AC-positive electrode by pre-lithiated treatment<sup>21,33</sup>. The typical charge/discharge curves of the two types of iMOF-based hybrid capacitors shown in Fig. 4a revealed that the voltage drop caused by applied current and internal resistance during the rest after the initial charging and discharging processes

was smaller for 4,4'-Bph(COOLi)<sub>2</sub>/AC cell than for 2,6-Naph(COOLi)<sub>2</sub>/AC cell, reflecting the low internal resistance of 4,4'-Bph(COOLi)<sub>2</sub>-negative electrode. Accordingly, the 4,4'-Bph(COOLi)<sub>2</sub>/AC cell exhibited a high-energy density of approximately 60 Wh L<sup>-1</sup> at a low discharge rate and maintained a high-energy density of 40 Wh L<sup>-1</sup> at a high discharge rate of approximately 45 C, which corresponds to a discharge of 1.2 min (Fig. 4b). The volumetric energy density of the proposed hybrid capacitor is much higher than those of previously reported hybrid capacitors (asymmetric electrode configuration), such as MnO<sub>2</sub>+ZnO core-shell nanorods/reduced graphene oxide (rGO) (0.23 Wh L<sup>-1</sup>)<sup>34</sup>, hydrogen-treated TiO<sub>2</sub> (H-TiO<sub>2</sub>) +MnO<sub>2</sub> core-shell nanowires/H-TiO<sub>2</sub>+carbon (0.3 Wh L<sup>-1</sup>)<sup>35</sup>, Nb<sub>2</sub>O<sub>5</sub> nanorod/AC (6.7 Wh L<sup>-1</sup>)<sup>36</sup>, 3D core-shell structured Ni(OH)<sub>2</sub>+MnO<sub>2</sub> with carbon nanotube composite/AC (10.9 Wh L<sup>-1</sup>)<sup>37</sup>, graphene/AC (22.3 Wh L<sup>-1</sup>)<sup>38</sup>, nano-Li<sub>4</sub>Ti<sub>5</sub>O<sub>12</sub>/AC (40 Wh L<sup>-1</sup>)<sup>39</sup>, Fe<sub>2</sub>O<sub>3</sub> encapsulated rGO scroll/AC (49.7 Wh L<sup>-1</sup>)<sup>40</sup>, or symmetric electrode configuration capacitor, such as Ti<sub>3</sub>C<sub>2</sub>T<sub>x</sub>+rGO (5%) symmetric cell (32.6 Wh L<sup>-1</sup>)<sup>41</sup>.

Plots of volumetric energy vs. power density for the hybrid capacitors are shown in Fig. 4c. These plots indicate that the iMOF-based hybrid capacitors exhibit higher energies and power densities than the graphite-based hybrid capacitor and EDLC. In the graphite-based capacitor, the excess capacity of the negative electrode is necessary to prevent the formation of fully charged graphite ( $C_6Li$ ) in order to facilitate Li dendroid deposition. On the other hand, the proposed negative electrode of iMOF inherently suppresses Li dendroid deposition because of the operating potential of 0.5–1.0 V vs.  $Li/Li^+$ . Thus, the iMOF-negative electrode enabled reduction in the excess capacity of the negative electrode and enhanced the energy density of the capacitor cell. Remarkably, at low temperature of 0 °C (Fig. 4b, d), the high-rate performance of 4,4'-Bph(COOLi)<sub>2</sub>/AC cell was better than that of 2,6-Naph(COOLi)<sub>2</sub>/AC cell at all rate conditions. As both hybrid capacitors had the same AC-positive electrodes, this difference in performance can be attributed to the negative electrodes.

With respect to the cycle test of iMOF-based hybrid capacitors using iMOF-based electrodes Li-pre-doped to DOD 50% (Fig. 4e), the capacity retention of 4,4'-Bph(COOLi)<sub>2</sub>/AC cell was 63% after 1000 cycles, lower than that of 2,6-Naph(COOLi)<sub>2</sub>/AC cell (82%). To address this issue, a 4,4'-Bph(COOLi)<sub>2</sub> electrode pre-doped with Li at DOD 80% was used. Using this electrode, the capacity retention of the 4,4'-Bph(COOLi)<sub>2</sub>/AC cell improved to 86% by retarding the use of shallow DOD with high charge/discharge polarization (Fig. 4e). The discharge curves during cycle (Supplementary Figure 8a, b) indicates that the capacity fading appears in the lower voltage region than the open-circuit voltage of ca. 2.3 V, which corresponds to  $Li^+$  adsorption reaction in the AC-positive electrode, and the capacity fading of the cell using the 4,4'-Bph(COOLi)<sub>2</sub>-negative electrode of DOD 50% is remarkable as compared with that of DOD 80%. The results of XRD and electrochemical reversibility of the 4,4'-Bph(COOLi)<sub>2</sub> electrode in 4,4'-Bph(COOLi)<sub>2</sub>/AC capacitor cell (DOD 80%) after 1000 cycles (Supplementary Figure 8c, d) suggested that there is no serious change in crystal structure and electrochemical reversibility of the after cycling 4,4'-Bph(COOLi)<sub>2</sub> electrode. Therefore, the factor of the capacity fading during the cycle of the proposed capacitor is a Li disappearance that contributes to charge and discharge processes rather than structural deterioration of the 4,4'-Bph(COOLi)<sub>2</sub>-negative electrode. The reason of the disappearance of  $Li^+$  contributing to the charge and discharge reaction is considered to be related to internal resistance of the 4,4'-Bph(COOLi)<sub>2</sub> electrode which affects the polarization shown in Fig. 2. The details of the internal resistance will be discussed later.

**Origin of high-rate capability of 4,4'-Bph(COOLi)<sub>2</sub>/AC cell.** To clarify the origin of the high-rate capability of the 4,4'-Bph(COOLi)<sub>2</sub> electrode, electrochemical impedance spectroscopy using symmetric cells (EIS-SC) was conducted with the lithiated 4,4'-Bph(COOLi)<sub>2</sub> and 2,6-Naph(COOLi)<sub>2</sub> electrodes. The symmetric cells were constructed from two identical electrodes assembled with a separator filled with electrolyte, allowing the EIS-SC analysis to focus on the impedance of a single electrode without affecting the other electrode<sup>42,43</sup>. In order to understand the DOD dependence of the internal resistance, we prepared symmetric cells comprising two identical 4,4'-Bph(COOLi)<sub>2</sub> electrodes lithiated to DOD 20%, 50%, and 80% respectively, and conducted EIS-SC analysis. The results are shown in Fig. 5a. The Nyquist plots at the lithiated electrodes showed a 45° slope to the real axis in the high-frequency region and a semicircle in the low-frequency region. By using the equivalent circuit of the transmission line models (see Methods and Supplementary Figure 9)<sup>42,43</sup>, the ionic resistance in pores ( $R_{ion}$ ) and charge-transfer resistance ( $R_{ct}$ ) were obtained from the fitting of the Nyquist plots

(Supplementary Figure 10). The size of the semicircle in the low-frequency region, which reflects that  $R_{ct}$  decreased with increasing DOD, indicates that the charge-transfer reaction of the 4,4'-Bph(COOLi)<sub>2</sub> is slow for shallow DOD. The trend in total internal resistance was in good agreement with the observed polarization behavior of the  $Li/4,4'$ -Bph(COOLi)<sub>2</sub> cells (Fig. 2a). The results of EIS suggest that the small polarization in deep DOD is derived from the decrease in the internal resistance related to the charge-transfer reaction at the 4,4'-Bph(COOLi)<sub>2</sub> electrode/electrolyte interface. Therefore, the pre-lithiated treatment leading to deep DOD is also important in the hybrid capacitors using proposed material in terms of improvement of power characteristics. Regarding the influence of the internal resistance on the cycle characteristics shown in Fig. 4e, since the negative electrode of DOD 50% utilizes the high internal resistance region, the amount of Li contributing to charge and discharge reaction disappears during cycling, thereby causing a decrease in cell capacity; in contrast, since the negative electrode of DOD 80% uses the low internal resistance region, the cycle characteristics are improved by suppressing the disappearance of the amount of Li.

The lithiated 2,6-Naph(COOLi)<sub>2</sub> and graphite electrodes at DOD 50% were also subjected to EIS-SC at a temperature of 20 °C for comparison with the 4,4'-Bph(COOLi)<sub>2</sub> electrode (Fig. 5b). The semicircle in the plot of the 4,4'-Bph(COOLi)<sub>2</sub> electrode was much smaller than that in the plot of the 2,6-Naph(COOLi)<sub>2</sub> electrode, indicating that the low  $R_{ct}$  of the 4,4'-Bph(COOLi)<sub>2</sub> electrode imparted high-rate capability to the capacitor cell. Remarkably, the graphite and 4,4'-Bph(COOLi)<sub>2</sub> electrodes generated similarly sized EIS-SC semicircles at 20 °C (Fig. 5b), whereas the semicircle of 4,4'-Bph(COOLi)<sub>2</sub> electrode was smaller than that of graphite at 0 °C (Fig. 5c). This indicates that the lower  $R_{ct}$  of 4,4'-Bph(COOLi)<sub>2</sub> led to better performance at low temperature.

The dependence of total internal resistance on temperature ( $1/3R_{ion} + R_{ct}$ ) calculated by fitting the Nyquist plots (Supplementary Figure 10) at temperatures ranging from -30 °C to 60 °C (Supplementary Figure 11) is shown in the Arrhenius plots in Fig. 5d. The activation energies ( $E_a$ ) for total internal resistance were calculated using the Arrhenius equation (see Methods). The  $E_a$  values of the 4,4'-Bph(COOLi)<sub>2</sub>, 2,6-Naph(COOLi)<sub>2</sub>, and graphite electrodes were 42.7, 47.3, and 49.1 kJ mol<sup>-1</sup>, respectively. The  $E_a$  of the 2,6-Naph(COOLi)<sub>2</sub> electrode was slightly lower than that of the graphite electrode, whereas the  $E_a$  of the 4,4'-Bph(COOLi)<sub>2</sub> electrode was much lower than those of the other two electrodes (Table 1). The favorable performance of the hybrid capacitors with 4,4'-Bph(COOLi)<sub>2</sub> electrodes at low temperatures can be attributed to the lower  $E_a$  of the charge-transfer resistance in this electrode. The  $E_a$  for the  $R_{ct}$  is dominated by the desolvation of solvated  $Li^+$  as the rate-determining step<sup>44–48</sup>; thus, the lower  $E_a$  values in iMOF electrodes suggest that the carboxylate groups of the iMOFs promote the desolvation of  $Li^+$  ions. Additionally, the distinct difference between the  $E_a$  values of the 2,6-Naph(COOLi)<sub>2</sub> and 4,4'-Bph(COOLi)<sub>2</sub> electrodes can be explained as follows. (i) The wider organic layer in the 4,4'-Bph(COOLi)<sub>2</sub> crystal structure enabled the intercalation process of partly solvated  $Li^+$  into the organic layer, decreasing the Gibbs energy required for desolvation<sup>23,44</sup>. (ii) The stepwise reaction in 4,4'-Bph(COOLi)<sub>2</sub> (Fig. 2b) decreased the activation energy of each reduction step, unlike the concerted reaction in 2,6-Naph(COOLi)<sub>2</sub><sup>49</sup>.

**Calculation of electron-hopping mobility.** To explain the favorable rate performance and low-temperature performance of the 4,4'-Bph(COOLi)<sub>2</sub> electrode, electronic-hopping mobility was calculated using the Marcus theory<sup>50,51</sup>. First-principles calculations were performed using a projector-augmented wave (PAW)

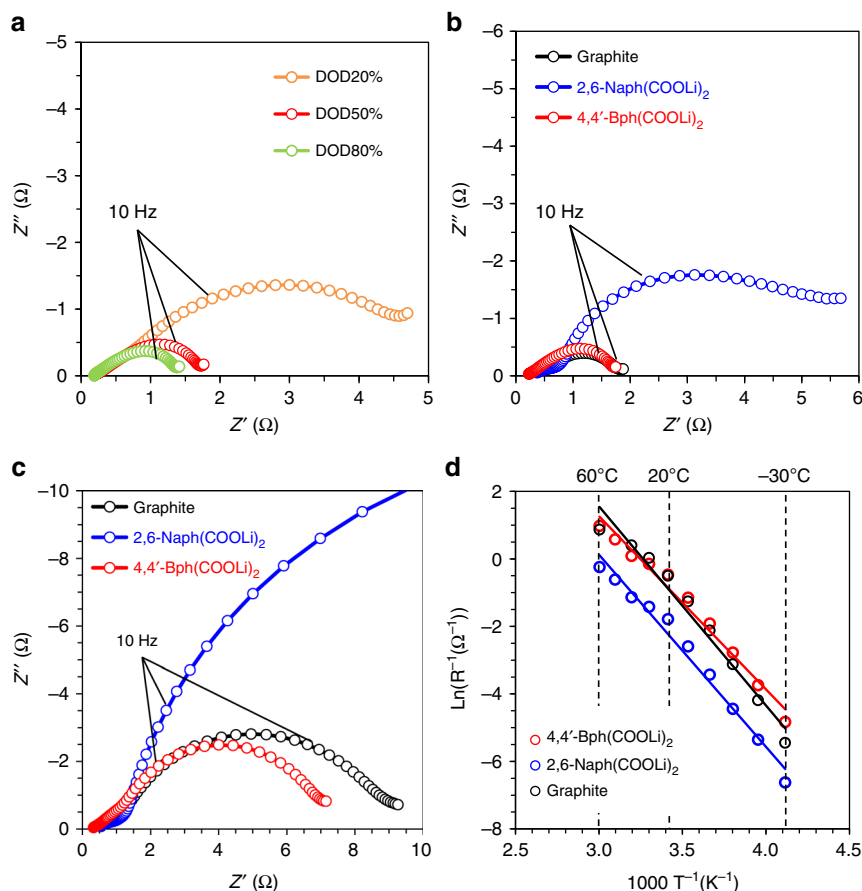


**Fig. 5** Analysis of internal resistance. **a** Nyquist plots for symmetric cells with two identical 4,4'-Bph(COOLi)<sub>2</sub> electrodes at DOD 20% (orange), 50% (red), and 80% (green) at 20 °C. **b, c** Nyquist plots of symmetric cells 2,6-Naph(COOLi)<sub>2</sub> (blue), 4,4'-Bph(COOLi)<sub>2</sub> (red), and graphite (black) electrodes at DOD 50% and 20 °C (**b**) and 0 °C (**c**). **d** Temperature dependence of  $1/3R_{\text{ion}} + R_{\text{ct}}$  in 2,6-Naph(COOLi)<sub>2</sub> (blue), 4,4'-Bph(COOLi)<sub>2</sub> (red), and graphite (black) electrodes lithiated up to DOD 50%

**Table 1** Activation energy ( $E_a$ ) for internal resistances

	$E_a$ (kJ mol <sup>-1</sup> )
2,6-Naph(COOLi) <sub>2</sub>	47.3
4,4'-Bph(COOLi) <sub>2</sub>	42.7
Graphite	49.1

method based on density functional theory implemented in the Vienna ab initio simulation package (VASP)<sup>52</sup> to determine the atomic positions of the Li intercalation state in Li<sub>2</sub>[Bph(COOLi)<sub>2</sub>] (Supplementary Figure 12). The optimized crystal structure of Li<sub>2</sub>[Bph(COOLi)<sub>2</sub>] shown in Supplementary Figure 12b indicates that the intercalated Li<sup>+</sup> ions were located adjacent to the LiO<sub>4</sub> network layers, forming a distorted triangular LiO<sub>2</sub>C structure. The intercalated Li<sup>+</sup> would be stabilized by the Li<sup>+</sup>-C<sup>δ-</sup> interaction of the negatively charged C atoms of biphenyl covalently bonded by a carboxylate group (Supplementary Figure 12c), as in 2,6-Naph(COOLi)<sub>2</sub><sup>19</sup>. The calculated lattice constants are summarized in Supplementary Table 2. The lattice constants along the *b*- and *c*-axes were shortened in Li intercalation state, indicating the shortening of the biphenyl  $\pi$ -stacking distance, which resulted in high electron mobility along the  $\pi$ -stacking direction.

To further investigate electron mobility between adjacent molecules, hopping conduction parameters such as transfer integral (*V*), reorganization energy ( $\lambda$ ), and drift mobility of hopping ( $\mu$ ) were calculated (see Methods). We considered the

following three hopping paths, as shown in Supplementary Figure 13: (i) face-to-face packing with  $\pi$ - $\pi$  interaction in a layered basal herringbone packing (P), (ii) face-to-edge packing (T), and (iii) edge-edge packing across the tetrahedral LiO<sub>4</sub> layer (L)<sup>32</sup>. The calculation results shown in Table 2 indicate that the values of  $\mu$  for Li<sub>2</sub>[Bph(COOLi)<sub>2</sub>] along the P, T, and L pathways were estimated to be quite larger conductivity than those for Li<sub>2</sub>[Naph(COOLi)<sub>2</sub>]<sup>32</sup>. This is because the  $\lambda$  value for Li<sub>2</sub>[Bph(COOLi)<sub>2</sub>] is smaller than that for Li<sub>2</sub>[Naph(COOLi)<sub>2</sub>]. Thus, the total  $\mu$  value for Li<sub>2</sub>[Bph(COOLi)<sub>2</sub>] (192 cm<sup>2</sup> V<sup>-1</sup> s<sup>-1</sup>) was also quite larger than that for Li<sub>2</sub>[Naph(COOLi)<sub>2</sub>] (8.25 cm<sup>2</sup> V<sup>-1</sup> s<sup>-1</sup>). The high electron-hopping mobility of 4,4'-Bph(COOLi)<sub>2</sub> contributed to its low charge-transfer resistance and good rate capability. Remarkably, although Li<sub>2</sub>[Naph(COOLi)<sub>2</sub>] showed a large value of  $\mu$  in path P and a small value in path T (6.49 and 0.85 cm<sup>2</sup> V<sup>-1</sup> s<sup>-1</sup>, respectively), indicating anisotropic two-dimensional (2D) electronic transport within the organic layer of Li<sub>2</sub>[Naph(COOLi)<sub>2</sub>], Li<sub>2</sub>[Bph(COOLi)<sub>2</sub>] showed large  $\mu$  values in both the P and T paths (35 and 75 cm<sup>2</sup> V<sup>-1</sup> s<sup>-1</sup>, respectively), indicating isotropic 2D electronic transport (Table 2).

The calculated three-dimensional (3D) electron density distribution of the conduction-band minimum in Li<sub>2</sub>[Bph(COOLi)<sub>2</sub>] crystal structure also indicates the existence of two electronic-hopping conduction pathways in the  $\pi$ -stacked face-to-face packing and face-to-edge packing directions of the biphenyl units (Fig. 6a). The electron delocalization between C1 and C2 (Fig. 6b) of 3D electron density distribution corresponds to the electron-hopping conduction in the face-to-edge packing

**Table 2** Parameter values for hopping mobility calculated from Marcus theory

		$\text{Li}_2[\text{Naph}(\text{COOLi})_2]^{32}$	$\text{Li}_2[\text{Bph}(\text{COOLi})_2]$
Reorganization energy $\lambda$ (eV)		0.423	0.107
Transfer integral $V$ (eV)	P	-1.11	-0.727
	T	-0.721	-0.871
	L	-0.264	-0.296
Drift mobility of hopping $\mu$ ( $\text{cm}^2 \text{V}^{-1} \text{s}^{-1}$ )	P	6.49	35
	T	0.85	75
	L	0.05	7.08
	Total	8.25	192

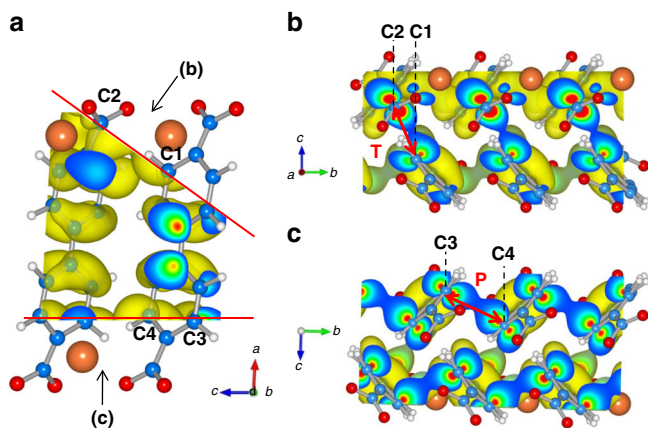


**Fig. 6** Predictive calculation of electron-hopping conduction. **a–c** 3D electron density distribution of the conduction-band minimum of the  $\text{Li}_2[\text{Bph}(\text{COOLi})_2]$  crystal structure calculated from the results using the PBEsol functional in the *b*-axis (**a**), in the upper *a*-axis (**b**), and in the bottom *a*-axis (**c**)

direction of path T, reflecting electron conduction along the *c*-axis direction. The electron delocalization between C3 and C4 (Fig. 6c) of 3D electron density distribution corresponds to the electron-hopping conduction in the  $\pi$ -stacked face-to-face packing direction of path P, reflecting electron conduction along the *b*-axis direction. The calculation result of the electron density distribution shows that  $\text{Li}_2[\text{Naph}(\text{COOLi})_2]$  reported previously is one electronic-hopping pass<sup>32</sup>, whereas  $\text{Li}_2[\text{Bph}(\text{COOLi})_2]$  shows two electronic-hopping passes (face-to-face and face-to-edge hopping paths). Therefore, this isotropic 2D electron transport within the organic layer of the  $4,4'$ -Bph(COOLi)<sub>2</sub> crystal enhances the electron-hopping mobility.

## Discussion

In this study, we applied a kind of iMOF material,  $4,4'$ -Bph(COOLi)<sub>2</sub>, for a negative electrode of hybrid capacitors. The prepared  $4,4'$ -Bph(COOLi)<sub>2</sub>/AC capacitor cell showed a high-energy density of approximately 60 Wh L<sup>-1</sup>, high-rate capability, favorable low-temperature performance, and good cycle durability. Impedance analysis of  $4,4'$ -Bph(COOLi)<sub>2</sub>-negative electrodes revealed that the low internal resistance of the  $4,4'$ -Bph(COOLi)<sub>2</sub> electrode is responsible for the high-rate capability, and the low activation energy for charge-transfer resistance in the  $4,4'$ -Bph(COOLi)<sub>2</sub> electrode explains the favorable low-temperature performance.

Calculation analyses indicated high electric conductivity in  $\text{Li}_2[\text{Bph}(\text{COOLi})_2]$  crystals in Li intercalation state because of the isotropic 2D electronic conduction with two electron-hopping pathways between adjacent molecules in the organic layer. The long biphenyl organic layer is thought to lead to the high Li<sup>+</sup> and

electronic conduction in the  $4,4'$ -Bph(COOLi)<sub>2</sub> crystal structure. Focusing on the relationship between the aromatic unit and the electrochemical reaction mechanism of the proposed materials, phenyl and naphthalene with a rigid structure show a concerted electron transfer<sup>19</sup>, whereas biphenyl with rotatable structure shows stepwise electron transfer. Our results in this study suggest that the biphenyl unit has a narrow indirect transition band structure related to small charge/discharge polarization. Therefore, the approach to further reduction of resistance requires design of molecular and its crystal structure considering electron density distribution and closely related band structure<sup>32</sup> in Li intercalation state. We hope that this research can stimulate further development of novel organic electrode materials and discovery of electrochemical performance which exceeds those of the conventional electrode materials.

## Methods

**Synthesis of  $4,4'$ -Bph(COOLi)<sub>2</sub>.** LiOH·H<sub>2</sub>O (3.812 g) was dissolved in 250 mL methanol, and 10.0 g  $4,4'$ -Bph(COOH)<sub>2</sub> was rapidly added to the methanol solution at room temperature under stirring. The obtained white suspension was stirred under reflux for 12 h. The mixture was evaporated, and the resulting solid was filtered, washed with methanol, and dried under ambient conditions; the product was obtained as powder (94% yield based on the amount of  $4,4'$ -Bph(COOH)<sub>2</sub> used).

**Characterization.** The pristine  $4,4'$ -Bph(COOLi)<sub>2</sub> sample was characterized by powder XRD followed by Rietveld refinement. The XRD pattern of the sample was obtained using Debye–Scherrer camera at the beamline 19B2 at SPring-8. The data were recorded with a curved imaging plate detector with a wavelength of 0.7000 Å for  $2\theta$  values of 5° to 35°; the step size was 0.01°. The data were recorded in transmission mode using a capillary tube filled with the sample. XRD data were refined using conventional Rietveld methods in the GSAS package with the EXPGUI interface<sup>53</sup>. The background, scale factor, zero point, lattice parameters, atomic positions, and coefficient of the peak-shape function were iteratively refined until convergence was achieved. The initial structure for Rietveld refinement was based on the previous paper<sup>27</sup>. The pristine and after cycling  $4,4'$ -Bph(COOLi)<sub>2</sub> electrodes were analyzed by ex situ XRD using a Rigaku RINT-TTR diffractometer with CuK $\alpha$  radiation at 50 kV and 300 mA in the  $2\theta_{\text{CuK}\alpha}$  range of 15°–35° in reflection mode under air atmosphere. Prior to ex situ XRD measurement, the after cycling electrode sample was taken from the  $4,4'$ -Bph(COOLi)<sub>2</sub>/AC cell.

SEM was performed using a Quanta 200 FEG microscope (Nikon Instech Co., Ltd.). Samples were sputtered with Pt and imaged at 15 keV using an electron gun.

The UV–vis spectra of 1,4-Ph(COOLi)<sub>2</sub>, 2,6-Naph(COOLi)<sub>2</sub>, and  $4,4'$ -Bph(COOLi)<sub>2</sub> powders were obtained with a Jasco V670 spectrometer (Nihon Bunko).

**Electrode and electrolyte preparations.** The  $4,4'$ -Bph(COOLi)<sub>2</sub> and 2,6-Naph(COOLi)<sub>2</sub> electrodes were prepared by coating a dispersion composed of 81.0 wt%  $4,4'$ -Bph(COOLi)<sub>2</sub> (or 2,6-Naph(COOLi)<sub>2</sub>), 14.3 wt% carbon black as a conductive additive, 1.9 wt% polyacrylic acid, and 2.8 wt% styrene butadiene rubber (SBR) in water onto Cu foil. Electrode loading weight of ca. 4 mg cm<sup>-2</sup> was used. AC-based electrodes were also prepared by coating a dispersion of 83 wt% AC (Kurare YP-20), 10.7 wt% carbon black, 4 wt% polyacrylic acid, and 2.3 wt% SBR in water onto Al foil. The electrode loading weight was ca. 3 mg cm<sup>-2</sup>. Graphite-based electrodes were prepared by coating a dispersion of 95 wt% graphite and 5 wt% polyvinylidene fluoride in *N*-methyl-2-pyrrolidone onto Cu foil. The electrode loading weight was ca. 4 mg cm<sup>-2</sup>. The electrolytes in this study were 1.0 M LiPF<sub>6</sub> dissolved in a mixed solvent of ethylene carbonate, dimethyl carbonate, and ethyl methyl carbonate (volume ratio = 30:40:30) for hybrid capacitors and 1.0 M triethylmethylammonium tetrafluoroborate dissolved in a solvent of propylene carbonate for EDLC.

**Electrochemical characterization.** The electrochemical properties of 4,4'-Bph(COOLi)<sub>2</sub> and 2,6-Naph(COOLi)<sub>2</sub> electrodes were evaluated using a coin-type cell with Li metal discs as counter electrodes and microporous polypropylene film saturated with electrolyte in an argon-filled glove box. For cyclic voltammetric measurements (Solartron 1470E, England), the redox response was carried out at scan rates of 0.015, 0.030, and 0.060 mV s<sup>-1</sup> within potential range of 0.5–1.5 V vs. Li/Li<sup>+</sup> at 25 °C, respectively. Galvanostatic charge–discharge tests were conducted at a rate corresponding to fully charging the theoretical capacity of the 4,4'-Bph(COOLi)<sub>2</sub> or 2,6-Naph(COOLi)<sub>2</sub> per 10 h (1/10 C rate) between 0.5 and 1.5 V vs. Li/Li<sup>+</sup> at 25 °C.

The evaluated hybrid capacitors were laminate-type single cells composed of AC-positive and pre-lithiated iMOF-negative electrodes with microporous polypropylene film separator saturated with the same electrolyte in an argon-filled glove box. Prior to galvanostatic charge–discharge measurements of the hybrid capacitors, 4,4'-Bph(COOLi)<sub>2</sub> electrodes were pre-lithiated by discharging laminate-type Li/4,4'-Bph(COOLi)<sub>2</sub> cells up to DOD 50% or DOD 80%. These proposed symmetric capacitors can utilize the high electric double-layer capacities combining both Li<sup>+</sup> cations and PF<sub>6</sub><sup>-</sup> anions at the AC-positive electrode by the pre-lithiated treatment. The 2,6-Naph(COOLi)<sub>2</sub> electrodes were pre-lithiated by discharging laminate-type Li/2,6-Naph(COOLi)<sub>2</sub> cells up to DOD 50%. The lithiated electrodes were taken out by disassembling the Li/iMOF cells, and the lithiated electrode and the AC electrode were reassembled. Optimization of the capacity ratio between the positive and the negative electrodes was performed referring to our previous study<sup>28</sup>. The graphite-based hybrid capacitor and EDLC (AC/AC cell) were also prepared in the same way for comparison. Galvanostatic charge–discharge measurements of the 4,4'-Bph(COOLi)<sub>2</sub>/AC or 2,6-Naph(COOLi)<sub>2</sub>/AC were conducted at 25 °C between 1.5 and 3.8 V at various rates between ca. 1 C and 50 C (ca. 1 and 100 mA cm<sup>-2</sup>, respectively) for rate capability test. The graphite/AC hybrid capacitors and EDLC were also conducted at 25 °C between 2.2 and 3.8 V, and 0.0 and 2.5 V, respectively, at various C rates. The cycle tests of 4,4'-Bph(COOLi)<sub>2</sub>/AC cells were conducted at a rate of 10 C. The volumetric energy (*E*) and power (*P*) densities were calculated from the obtained electrochemical characteristics according to the following equations:

$$E = \int IV(t)dt/V_{\text{electrodes}} \quad (2)$$

$$P = E/\Delta t, \quad (3)$$

where *I*, *V*(*t*), *V*<sub>electrodes</sub> and *Δt* are the constant current, working voltage, the total electrode volume, and discharge time, respectively. The *V*<sub>electrodes</sub> in this study was calculated from the electrode area and the electrode thickness for both positive and negative electrodes not including the current collector.

AC impedance measurements (Solartron 1400A/1470E, England) were performed using laminate-type single symmetric cells composed of two lithiated iMOF electrodes with a microporous polypropylene film separator saturated with the same electrolyte in an argon-filled glove box<sup>42,43</sup>. Prior to AC impedance measurements, the iMOF electrodes were pre-lithiated by discharging the laminate-type Li/iMOF cells up to DOD 20%, 50%, and 80% for 4,4'-Bph(COOLi)<sub>2</sub> electrodes and DOD 50% for 2,6-Naph(COOLi)<sub>2</sub> electrodes. The lithiated electrodes were taken out by disassembling the Li/iMOF cells, and the two lithiated electrodes were reassembled into the symmetric cells in an argon-filled glove box. The *R*<sub>ct</sub> values of the iMOF electrodes were determined by measurements of faradaic processes in the symmetric cells with DOD 50% iMOF electrodes. The frequency was varied from 100 kHz to 100 mHz with a perturbation amplitude of 10 mV (peak to peak). Measurements were performed at open-circuit potential and between -30 °C and 60 °C. Experimental impedance fitting of the symmetric cell data was carried out using Zview software (Scribner Associates, Inc., USA). The equivalent circuit for fitting the impedance spectra at DOD 0 and 50% used the generalized finite-length Warburg element open-circuit terminus (*W*<sub>o</sub>) and short-circuit terminus (*W*<sub>s</sub>) for descriptive purposes (Supplementary Figure 9), respectively<sup>54,55</sup>. *R*<sub>ion</sub> and *R*<sub>ct</sub> were calculated from the resistance values obtained by fitting using following Eqs. (9) and (10).

**Calculation of direct and indirect bandgaps from the results of UV-vis spectra.** The optical absorption near the band edge follows the equation<sup>56</sup>:

$$\alpha hv = A \left( hv - E_g \right)^{n/2}, \quad (4)$$

where *α*, *ν*, *A*, and *E*<sub>g</sub> are absorption coefficient, light frequency, proportionality constant, and bandgap, respectively. In the equation, *n* decides the characteristics of the transition in a semiconductor as direct adsorption (*n* = 1, Eq. (5)) and indirect adsorption (*n* = 4, Eq. (6)) follows the equations, respectively:

$$(\alpha hv/A)^2 = hv - E_g. \quad (5)$$

$$(\alpha hv/A)^{1/2} = hv - E_g. \quad (6)$$

Direct and indirect bandgaps (*E*<sub>g</sub>) are obtained from the straight-line approximation of (*αhv*)<sup>2</sup> and (*αhv*)<sup>1/2</sup> to *hν* corresponding to Eqs. (5) and (6), respectively.

**Impedance theory for cylindrical pores according to the transmission line model.**

For non-faradaic and faradaic processes in porous electrodes (the equivalent circuits according to the processes are shown in Supplementary Figure 9), the overall impedance is expressed by Eqs. (7) and (8), respectively<sup>42,43</sup>:

$$Z_{\text{non-faradaic},\omega} = \sqrt{\frac{R_{\text{ion},L}}{j\omega C_{\text{dl},A} 2\pi r}} \coth \sqrt{R_{\text{ion},L} \cdot j\omega C_{\text{dl},A} 2\pi r L}, \quad (7)$$

and

$$Z_{\text{faradaic},\omega} = \sqrt{\frac{R_{\text{ion},L} R_{\text{ct},A}}{(1 + j\omega R_{\text{ct},A} C_{\text{dl},A}) \cdot 2\pi r}} \coth \sqrt{\frac{R_{\text{ion},L} \cdot (1 + j\omega R_{\text{ct},A} C_{\text{dl},A}) 2\pi r}{R_{\text{ct},A}}} L, \quad (8)$$

where *R*<sub>ion,L</sub>, *C*<sub>dl,A</sub>, *r*, *A* and *L* are ionic resistance per unit pore length, electric double-layer capacitance per unit surface area, pore radius, surface area per unit, and pore length per unit, respectively. The limiting values of the real term *Z'*<sub>ω</sub> as *ω* → 0 for the non-faradaic and faradaic processes are given by Eqs. (9) and (10), respectively:

$$Z'_{\text{non-faradaic},\omega \rightarrow 0} = \frac{R_{\text{ion}}}{3}, \quad (9)$$

and

$$Z'_{\text{faradaic},\omega \rightarrow 0} = \frac{R_{\text{ion}}}{3} + R_{\text{ct}}, \quad (10)$$

where *R*<sub>ion</sub> is a characteristic parameter that expresses the ionic resistance inside the porous electrode, and *R*<sub>ct</sub> is the charge-transfer resistance for the lithium intercalation reaction.

**Kinetic interpretation of internal resistance of individual electrodes.** The activation energies (*E*<sub>a</sub>) for total internal resistance were calculated using the Arrhenius equation as follows<sup>42</sup>:

$$\frac{1}{R_x} = A \exp\left(-\frac{E_a}{RT}\right), \quad (11)$$

where *A*, *E*<sub>a</sub>, *R*, and *T* are the frequency factor, activation energy, gas constant, and absolute temperature, respectively.

**Structural optimization using first-principles calculations.** The crystal structures of 4,4'-Bph(COOLi)<sub>2</sub> and Li<sub>2</sub>[Bph(COOLi)<sub>2</sub>] were optimized via first-principles calculations in VASP<sup>52</sup> using the PAW method. The cutoff energy for the plane waves was set to 500 eV, and the *k*-point grid for the integral over the Brillouin zone was approximately divided into 0.01 Å<sup>-1</sup>. Gaussian smearing with a width of 0.2 eV was adopted during optimization. The atomic positions were optimized until the atomic forces became smaller than 0.01 eV Å<sup>-1</sup>. For the exchange-correlation energy within density functional theory, the PBEsol functional<sup>57</sup>, which revises the Perdew–Burke–Ernzerhof generalized gradient approximation functional to improve the equilibrium properties of solids and surfaces, was applied.

**Calculation of electron-hopping mobility using Marcus theory.** Marcus theory<sup>50,51,58</sup> was applied to calculate the electron-hopping mobility in 4,4'-Bph(COOLi)<sub>2</sub> and Li<sub>2</sub>[Bph(COOLi)<sub>2</sub>]. The electron-hopping rate between neighboring molecules (*W*) can be determined based on the Marcus theory as shown below:

$$W = \frac{V^2}{\hbar} \left( \frac{\pi}{\lambda k_B T} \right)^{1/2} \exp\left(-\frac{\lambda}{4k_B T}\right), \quad (12)$$

where *V* is the transfer integral between the initial and final states (eV), *λ* is the reorganization energy, which is defined as the energy change associated with the geometry relaxation during charge transfer, *ħ* is Planck's constant, and *k*<sub>B</sub> is the Boltzmann constant. The diffusion coefficient (*D*) is calculated from the hopping rates (cm<sup>2</sup> s<sup>-1</sup>) as

$$D = \frac{1}{2n} \sum_i r_i^2 W_i P_i, \quad (13)$$

where  $n$  is the dimensionality,  $i$  represents a specific hopping pathway,  $r_i$  is the hopping distance between two molecules, and  $P_i$  is the hopping mobility, which is calculated by

$$P_i = \frac{W_i}{\sum_i W_i} \quad (14)$$

The drift mobility of hopping ( $\mu$ ) can then be evaluated from the Einstein relation ( $\text{cm}^2 \text{V}^{-1} \text{s}^{-1}$ ),

$$\mu = \frac{e}{k_B T} D, \quad (15)$$

where  $e$  is electronic charge. Intermolecular transfer integrals and reorganization energies were calculated using the site-energy correction method<sup>59</sup> and the dimer projection (DIPRO) approach<sup>60</sup>. The details of the calculation scheme can be found in our previous report<sup>32</sup>. The electron-hopping rate was calculated for the  $\text{C}_{12}\text{H}_8\text{O}_4\text{Li}_2(\text{Li}_2)$  molecules extracted from the computed optimized structures of 4,4'-Bph(COOLi<sub>2</sub>) and Li<sub>2</sub>[4,4'-Bph(COOLi<sub>2</sub>)] using the Gaussian 09 package<sup>61</sup> with the B3LYP functional and the 6-311++G\* basis set.

## Data availability

The authors declare that all the other data supporting the findings of this study are available within the article and its supplementary information files and from the corresponding author upon request.

Received: 28 March 2018 Accepted: 20 September 2018

Published online: 19 October 2018

## References

- Burke, A. R&D considerations for the performance and application of electrochemical capacitors. *Electrochim. Acta* **53**, 1083–1091 (2007).
- Onar, O. C., Uzunoglu, M. & Alam, M. S. Dynamic modeling, design and simulation of a wind/fuel cell/ultra-capacitor-based hybrid power generation system. *J. Power Sources* **161**, 707–722 (2006).
- Beidaghi, M. & Gogotsi, Y. Capacitive energy storage in micro-scale devices: recent advances in design and fabrication of micro-supercapacitors. *Energy Environ. Sci.* **7**, 867–884 (2014).
- Pell, W. G. & Conway, B. E. Peculiarities and requirements of asymmetric capacitor devices based on combination of capacitor and battery-type electrodes. *J. Power Sources* **136**, 334–345 (2004).
- Beguín, F., Presser, V., Balducci, A. & Frackowiak, E. Carbons and electrolytes for advanced supercapacitors. *Adv. Mater.* **26**, 2283 (2014).
- Sivakkumar, S. R. & Pandolfo, A. G. Evaluation of lithium-ion capacitors assembled with pre-lithiated graphite anode and activated carbon cathode. *Electrochim. Acta* **65**, 280–287 (2012).
- Lukatskaya, M. R., Dunn, B. & Gogotsi, Y. Multidimensional materials and device architectures for future hybrid energy storage. *Nat. Commun.* **7**, 12647 (2016).
- Plitz, I. et al. The design of alternative nonaqueous high power chemistries. *Appl. Phys. A* **82**, 615–626 (2005).
- Park, G., Gunawardhana, N., Nakamura, H., Lee, Y.-S. & Yoshio, M. The study of electrochemical properties and lithium deposition of graphite at low temperature. *J. Power Sources* **199**, 293–299 (2012).
- Ogihara, N. Nonaqueous secondary battery electrode, nonaqueous secondary battery including the same, and assembled battery. Japanese patent no. WO2012/053553 (2014).
- Ogihara, N. Nonaqueous secondary battery electrode, nonaqueous secondary battery including the same, and assembled battery. US patent no. 20130136972 (2011).
- Armand, M. et al. Conjugated dicarboxylate anodes for Li-ion batteries. *Nat. Mater.* **8**, 120–125 (2009).
- Walker, W. et al. Electrochemical characterization of lithium 4,4'-tolenedicarboxylate for use as a negative electrode in Li-ion batteries. *J. Mater. Chem.* **21**, 1615 (2011).
- Park, Y. et al. Sodium terephthalate as an organic anode material for sodium ion batteries. *Adv. Mater.* **24**, 3562–3567 (2012).
- Choi, A. et al. 4,4'-Biphenyldicarboxylate sodium coordination compounds as anodes for Na-ion batteries. *J. Mater. Chem. A* **2**, 14986 (2014).
- Fedele, L., Sauvage, F., Bois, J., Tarascon, J. M. & Becuwe, M. Lithium insertion / de-insertion properties of  $\pi$ -extended naphthyl-based dicarboxylate electrode synthesized by freeze-drying. *J. Electrochem. Soc.* **161**, A46–A52 (2014).
- Häupler, B., Wild, A. & Schubert, U. S. Carbonyls: powerful organic materials for secondary batteries. *Adv. Energy Mater.* **5**, 1402034 (2015).
- Wang, C. et al. Extended  $\pi$ -conjugated system for fast-charge and -discharge sodium-ion batteries. *J. Am. Chem. Soc.* **137**, 3124–3130 (2015).
- Ogihara, N. et al. Organic dicarboxylate negative electrode materials with remarkably small strain for high-voltage bipolar batteries. *Angew. Chem. Int. Ed.* **53**, 11467–11472 (2014).
- Yasuda, T. & Ogihara, N. Reformation of organic dicarboxylate electrode materials for rechargeable batteries by molecular self-assembly. *Chem. Commun.* **50**, 11565–11567 (2014).
- Ogihara, N., Ozawa, Y. & Hiruta, O. A self-assembled intercalated metal-organic framework electrode with outstanding area capacity for high volumetric energy asymmetric capacitors. *J. Mater. Chem. A* **4**, 3398–3405 (2016).
- Ogihara, N. & Kishida, Y. Improvement in the electrochemical properties of intercalated metal-organic framework electrode materials by controlling crystal growth. *Electrochemistry* **83**, 861–863 (2015).
- Fédèle, L. et al. 2D-layered lithium carboxylate based on biphenyl core as negative electrode for organic lithium-ion batteries. *Chem. Mater.* **29**, 546–554 (2017).
- Liu, N., Li, H., Jiang, J., Huang, X. & Chen, L. Li–Biphenyl–1,2-dimethoxyethane solution: calculation and its application. *J. Phys. Chem. B* **110**, 10341–10347 (2006).
- de la Viuda, M., Yus, M. & Guíjarro, A. On the nature of lithium biphenyl in etheral solvents. A critical analysis unifying DFT calculations, physicochemical data in solution, and a X-ray structure. *J. Phys. Chem. B* **115**, 14610–14616 (2011).
- Funston, A. M., Lymar, S. V., Saunders-Price, B., Czapski, G. & Miller, J. R. Rate and driving force for protonation of aryl radical anions in ethanol. *J. Phys. Chem. B* **111**, 6895–6902 (2007).
- Banerjee, D., Borkowski, L. A., Kim, S. J. & Parise, J. B. Synthesis and structural characterization of lithium-based metal-organic frameworks. *Cryst. Growth Des.* **9**, 4922–4926 (2009).
- Zhu, Y. & Wang, C. Galvanostatic intermittent titration technique for phase-transformation electrodes. *J. Phys. Chem. C* **114**, 2830–2841 (2010).
- Hurd, C. D. & Oliver, G. L. The cleavage of phenyl alkyl ethers and O-heterocyclic compounds by sodium in liquid ammonia. *J. Am. Chem. Soc.* **81**, 2795–2798 (1959).
- Melero, C., Pérez, H., Guíjarro, A. & Yus, M. Reductive dearomatization of biphenyl: sequential one-pot regioselective introduction of two different electrophiles. *Tetrahedron Lett.* **48**, 4105–4109 (2007).
- Ito, S. et al. Bishexa-peri-hexabenzocoronene: a “Superbiphenyl”. *J. Am. Chem. Soc.* **122**, 7698–7706 (2000).
- Ogihara, N., Ohba, N. & Kishida, Y. On/off switchable electronic conduction in intercalated metal-organic frameworks. *Sci. Adv.* **3**, e1603103 (2017).
- Shiraiishi, S., Kurihara, H., Shi, L., Nakayama, T. & Oya, A. Electric double-layer capacitance of meso/macroporous activated carbon fibers prepared by the blending method - I. Nickel-loaded activated carbon fibers in propylene carbonate solution containing LiClO<sub>4</sub> salt. *J. Electrochem. Soc.* **149**, A855–A861 (2002).
- Zilong, W., Zhu, Z., Qiu, J. & Yang, S. High performance flexible solid-state asymmetric supercapacitors from MnO<sub>2</sub>/ZnO core-shell nanorods/specially reduced graphene oxide. *J. Mater. Chem. C* **2**, 1331–1336 (2014).
- Lu, X. et al. H-TiO<sub>2</sub>@MnO<sub>2</sub>/H-TiO<sub>2</sub>@C core-shell nanowires for high performance and flexible asymmetric supercapacitors. *Adv. Mater.* **25**, 267–272 (2013).
- Deng, B., Lei, T., Zhu, W., Xiao, L. & Liu, J. In-plane assembled orthorhombic Nb<sub>2</sub>O<sub>5</sub> nanorod films with high-rate Li<sup>+</sup> intercalation for high-performance flexible Li-ion capacitors. *Adv. Funct. Mater.* **28**, 1704330 (2018).
- Shen, J. et al. An asymmetric supercapacitor with both ultra-high gravimetric and volumetric energy density based on 3D Ni(OH)<sub>2</sub>/MnO<sub>2</sub>@carbon nanotube and activated polyaniline-derived carbon. *ACS Appl. Mater. Interfaces* **9**, 668–676 (2017).
- Zheng, C., Zhou, X., Cao, H., Wang, G. & Liu, Z. Synthesis of porous graphene/activated carbon composite with high packing density and large specific surface area for supercapacitor electrode material. *J. Power Sources* **258**, 290–296 (2014).
- Naoui, K., Ishimoto, S., Isobe, Y. & Aoyagi, S. High-rate nano-crystalline Li<sub>4</sub>Ti<sub>5</sub>O<sub>12</sub> attached on carbon nano-fibers for hybrid supercapacitors. *J. Power Sources* **195**, 6250–6254 (2010).
- Rani, J. R. et al. High volumetric energy density hybrid supercapacitors based on reduced graphene oxide scrolls. *ACS Appl. Mater. Interfaces* **9**, 22398–22407 (2017).
- Yan, J. et al. Flexible MXene/graphene films for ultrafast supercapacitors with outstanding volumetric capacitance. *Adv. Funct. Mater.* **27**, 1701264 (2017).
- Ogihara, N. et al. Theoretical and experimental analysis of porous electrodes for lithium-ion batteries by electrochemical impedance spectroscopy using a symmetric cell. *J. Electrochem. Soc.* **159**, A1034–A1039 (2012).
- Ogihara, N., Itou, Y., Sasaki, T. & Takeuchi, Y. Impedance spectroscopy characterization of porous electrodes under different electrode thickness using

- a symmetric cell for high-performance lithium-ion batteries. *J. Phys. Chem. C* **119**, 4612–4619 (2015).
44. Abe, T., Fukuda, H., Iriyama, Y. & Ogumi, Z. Solvated Li-ion transfer at interface between graphite and electrolyte. *J. Electrochem. Soc.* **151**, A1120–A1123 (2004).
45. Abe, T., Sagane, F., Ohtsuka, M., Iriyama, Y. & Ogumi, Z. Lithium-ion transfer at the interface between lithium-ion conductive ceramic electrolyte and liquid electrolyte—a key to enhancing the rate capability of lithium-ion batteries. *J. Electrochem. Soc.* **152**, A2151–A2154 (2005).
46. Yamada, Y., Iriyama, Y., Abe, T. & Ogumi, Z. Kinetics of lithium ion transfer at the interface between graphite and liquid electrolytes: effects of solvent and surface film. *Langmuir* **25**, 12766–12770 (2009).
47. Xu, K., von Cresce, A. & Lee, U. Differentiating contributions to “ion transfer” barrier from interphasial resistance and Li<sup>+</sup> desolvation at electrolyte/graphite interface. *Langmuir* **26**, 11538–11543 (2010).
48. Xu, K., Lam, Y., Zhang, S. S., Jow, T. R. & Curtis, T. B. Solvation sheath of Li<sup>+</sup> in nonaqueous electrolytes and its implication of graphite/electrolyte interface chemistry. *J. Phys. Chem. C* **111**, 7411–7421 (2007).
49. Evans, D. H. One-electron and two-electron transfers in electrochemistry and homogeneous solution reactions. *Chem. Rev.* **108**, 2113–2144 (2008).
50. Deng, W.-Q. & Goddard, W. A. Predictions of hole mobilities in oligoacene organic semiconductors from quantum mechanical calculations. *J. Phys. Chem. B* **108**, 8614–8621 (2004).
51. Kobayashi, H. et al. Hopping and band mobilities of pentacene, rubrene, and 2,7-dioctyl[1]benzothieno[3,2-b][1]benzothiophene (C<sub>8</sub>-BTBT) from first principle calculations. *J. Chem. Phys.* **139**, 014707 (2013).
52. Kresse, G. & Furthmüller, J. Efficient iterative schemes for *ab initio* total-energy calculations using a plane-wave basis set. *Phys. Rev. B* **54**, 11169–11186 (1996).
53. Toby, B. EXPGUI, a graphical user interface for GSAS. *J. Appl. Crystallogr.* **34**, 210–213 (2001).
54. Jang, J. H. & Oh, S. M. Complex capacitance analysis of porous carbon electrodes for electric double-layer capacitors. *J. Electrochem. Soc.* **151**, A571–A577 (2004).
55. Sugimoto, W., Iwata, H., Yokoshima, K., Murakami, Y. & Takasu, Y. Proton and electron conductivity in hydrous ruthenium oxides evaluated by electrochemical impedance spectroscopy: the origin of large capacitance. *J. Phys. Chem. B* **109**, 7330–7338 (2005).
56. Yi, Z. et al. An orthophosphate semiconductor with photooxidation properties under visible-light irradiation. *Nat. Mater.* **9**, 559–564 (2010).
57. Perdew, J. P. et al. Restoring the density-gradient expansion for exchange in solids and surfaces. *Phys. Rev. Lett.* **100**, 136406 (2008).
58. Li, H., Zheng, R. & Shi, Q. Theoretical study of charge carrier transport in organic semiconductors of tetrathiafulvalene derivatives. *J. Phys. Chem. C* **116**, 11886–11894 (2012).
59. Valeev, E. F., Coropceanu, V., da Silva Filho, D. A., Salman, S. & Brédas, J.-L. Effect of electronic polarization on charge-transport parameters in molecular organic semiconductors. *J. Am. Chem. Soc.* **128**, 9882–9886 (2006).
60. Baumeier, B., Kirkpatrick, J. & Andrienko, D. Density-functional based determination of intermolecular charge transfer properties for large-scale morphologies. *Phys. Chem. Chem. Phys.* **12**, 11103–11113 (2010).
61. M. J. Frisch et al. *Gaussian 09, Revision B.01* (Gaussian, Inc., Wallingford CT, 2010).

## Acknowledgements

The synchrotron radiation experiments were performed on BL19B2 at SPring-8 with the approval of the Japan Synchrotron Radiation Research Institute (JASRI) (Proposal No. 2012A1785). We acknowledge Dr. Y. Goto for UV-vis measurements.

## Author contributions

N.Og. conceived and designed the study. N.Og. and Y.O. prepared the manuscript and performed the electrochemical experiments. Y.K. performed XRD measurements. M.H. performed SEM experiments. O.H. prepared the electrode. N.Oh. performed the calculations for the hopping conduction.

## Additional information

**Supplementary information** accompanies this paper at <https://doi.org/10.1038/s42004-018-0064-5>.

**Competing interests:** The authors declare no competing interests.

**Reprints and permission** information is available online at <http://npg.nature.com/reprintsandpermissions/>

**Publisher's note:** Springer Nature remains neutral with regard to jurisdictional claims in published maps and institutional affiliations.



**Open Access** This article is licensed under a Creative Commons Attribution 4.0 International License, which permits use, sharing, adaptation, distribution and reproduction in any medium or format, as long as you give appropriate credit to the original author(s) and the source, provide a link to the Creative Commons license, and indicate if changes were made. The images or other third party material in this article are included in the article's Creative Commons license, unless indicated otherwise in a credit line to the material. If material is not included in the article's Creative Commons license and your intended use is not permitted by statutory regulation or exceeds the permitted use, you will need to obtain permission directly from the copyright holder. To view a copy of this license, visit <http://creativecommons.org/licenses/by/4.0/>.

© The Author(s) 2018